Thermal Flow Sensor With a Bidirectional Thermal Reference

Yuki Okamoto, *Member, IEEE*, Thanh-Vinh Nguyen, Hironao Okada, and Masaaki Ichiki

***Abstract*— Conventional thermal flow sensors require samples to be heated; however, the temperature rise of the measuring tools limits their use in biological applications. To address this limitation, in this study, we propose a thermal flow sensor with a bidirectional thermal reference. We fabricated an integrated calorimetric and hot-film thermal flow sensor with a bidirectional thermal reference using a Peltier module to produce a thermal distribution that depends on the flow rate. The integrated thermal flow sensors enable high-resolution and wide-range flow rate measurements in a microfluidic device without the use of heating reagents in the cooling measurement mode. In addition, the sensor can be used as a typical heating thermal flow sensor by inverting the current applied to the Peltier module. Computational fluid dynamics simulations and experiments were performed to evaluate the performance of the integrated sensors in heating and cooling modes. In both modes, the calorimetric sensor measured low flow rates with a resolution of 100 nL/min, whereas the hot-film sensor measured a wide range of flow rates up to 200 μL/min. The proposed sensor expands the use of the thermal flow sensors by switching between the cooling and heating modes according to the sample temperature and maximum temperature limit. [2022-0090]**

***Index Terms*— Thermal flow sensor, microfluidics, Peltier module, calorimetric, hot film.**

I. Introduction

MICROFLUIDIC technology based on microelectromechanical systems (MEMS) has gained significant interest for a wide range of applications. This technology has significantly enhanced lab-on-a-chip (LOC) devices and micro total analysis systems (μTAS), which are commonly used in chemical and biological research [1], [2], because such miniaturized devices facilitate analyses using small reagents and therefore replace bulky laboratory equipment.

Microfabricated components have been integrated into microfluidic devices and implemented to develop more complex LOC devices for point-of-care testing. This integration enables the size reduction of essential equipment using integrated microfluidic components, such as electrokinetic actuators [3], micropumps [4], [5], electrical circuits [6]–[8], and analytical sensors [7]–[17].

Importantly, integrated micromachined flow sensors have played an essential role in the development of LOC devices. Since the fabrication of micromachined flow sensors in 1974 [18], [19], many measurement principles for integrated flow sensors have been developed. Integrated flow sensors determine gas and liquid flow rates [7]–[10] and other flow parameters, such as viscosity [11], temperature [12], and surface potential [13]. Among these integrated flow sensors, thermal flow sensors are commonly used in LOC devices owing to their simple structure and compatibility with MEMS-process [7]–[9], [14], [15]. Thermal flow sensors utilize the thermal interaction between the sensor elements and the fluid. A symmetric thermal distribution is formed using a thermal reference, and when a flow exists, the convection cooling effect changes the thermal distribution and temperature. The sensing elements measure the temperature changes and derive the flow rate from the measured temperature. As the sensing elements in thermal flow sensors can precisely measure the temperature using microfabricated components, they can measure a wide range of flow rates with high resolution. Therefore, thermal flow sensors have great potential for measuring small amounts of reagents in biological LOC applications. However, typical thermal sensors require a microheater to create a thermal distribution. The heat reference increases the reagent temperature and causes damage to biological reagents. For instance, it is known that cell damage occurs at 42°C [20], and hence, the working temperature has to be set lower than the maximum safe temperature. Therefore, biological or medical analyses typically use other types of flow sensors, such as complicated laser doppler flow sensors [16]. Although these flow sensors do not harm biological samples, their resolution is notably less than that of thermal flow sensors.

In this study, we propose a novel thermal-flow sensor in which the thermal reference consists of a Peltier module. Using the cooling effect of the Peltier module, the reagent temperature can be maintained to be lower than the initial temperature, as demonstrated in our previous work [21]. However, the cooling operation affects the sample status when the initial sample temperature is too low. In such a case, the heating thermal flow sensor is more appropriate. Therefore, a bidirectional thermal flow sensor is required to handle both scenarios. In our study, we realized a thermal flow sensor that has a bidirectional thermal reference. The sensor can be used as a heating thermal flow sensor in the heating mode by switching the direction of the applied current to the Peltier module. It enables us to select the appropriate operating mode depending on the sample temperature and maximum temperature limit. We analyzed the temperature change in the cooling and heating modes using computational fluid dynamics (CFD) simulations and experimentally demonstrated both modes using the same device.

Manuscript received 19 May 2022; revised 26 July 2022; accepted 27 July 2022. Date of publication 4 August 2022; date of current version 3 October 2022. This work was supported by JSPS KAKENHI Grant Numbers JP20K22422 and JP21K14219. Subject Editor Y. Zohar. *(Corresponding author: Yuki Okamoto.)*

The authors are with the Sensing System Research Center, National Institute of Advanced Industrial Science and Technology (AIST), Tsukuba, Ibaraki 305-8564, Japan (e-mail: yuki.okamoto@aist.go.jp).

Color versions of one or more figures in this article are available at https://doi.org/10.1109/JMEMS.2022.3195169.

Digital Object Identifier 10.1109/JMEMS.2022.3195169

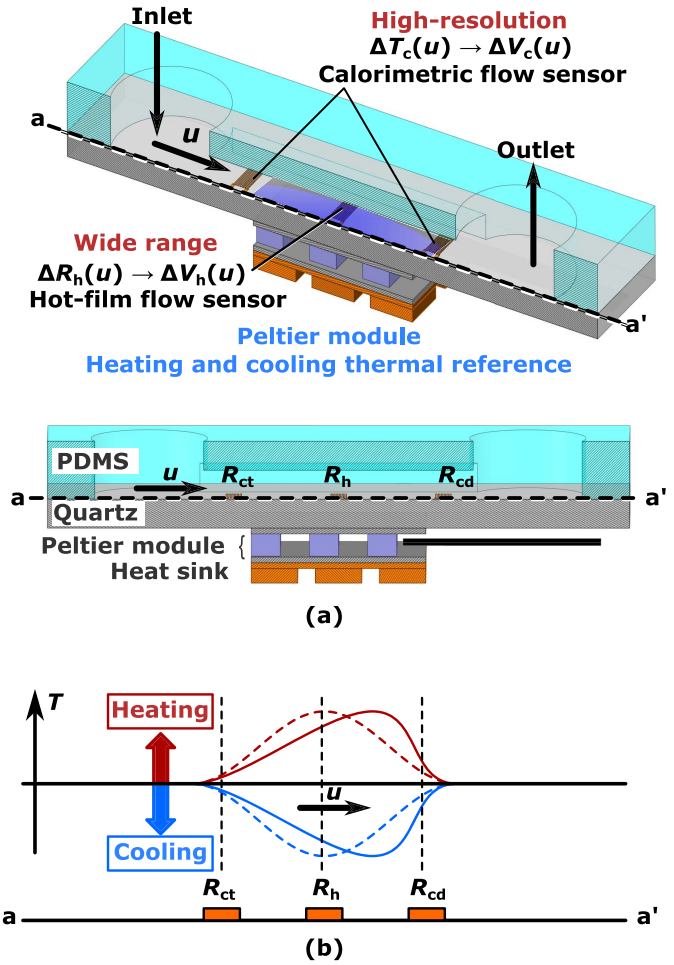

Fig. 1. (a) Schematic of the proposed cooling thermal flow sensor using a bidirectional thermal reference. (b) Cross-sectional view of the proposed flow sensor and the thermal distribution of conventional and proposed flow sensors.

II. Concept

Figure 1 shows a schematic of the proposed cooling thermal flow sensor. As shown in Fig. 1(a), the proposed flow sensor measures the flow rate by measuring the change in the thermal cooling distribution with thermo-resistances. The proposed sensor consists of a cooling thermal reference and thermo-resistances for hot-film (R_{h}) and calorimetric (R_{ct} and R_{cd}) measurements for high-resolution and wide-range sensing. The thermal reference was generated using a Peltier module attached to the bottom of the microfluidic chip. As seen in Fig. 1(b), the conventional thermal flow sensor changes the thermal flow distribution using the heater, while the proposed sensor creates the thermal flow distribution using the cooling effect within the cooling mode. The asymmetric thermal distribution increases the resistance of R_{ct} and R_{h} and reduces the resistance of R_{cd}. The relationship between resistance (R) and temperature (T) with respect to the flow (u) is expressed as follows:

$$R(T) = R(T_0)[1 + \alpha(T - T_0)], \tag{1}$$

where α is the temperature coefficient of resistance (TCR). Both hot-film and calorimetric sensors measure this thermo-resistive effect. As shown in Fig. 1(c), the wide-range

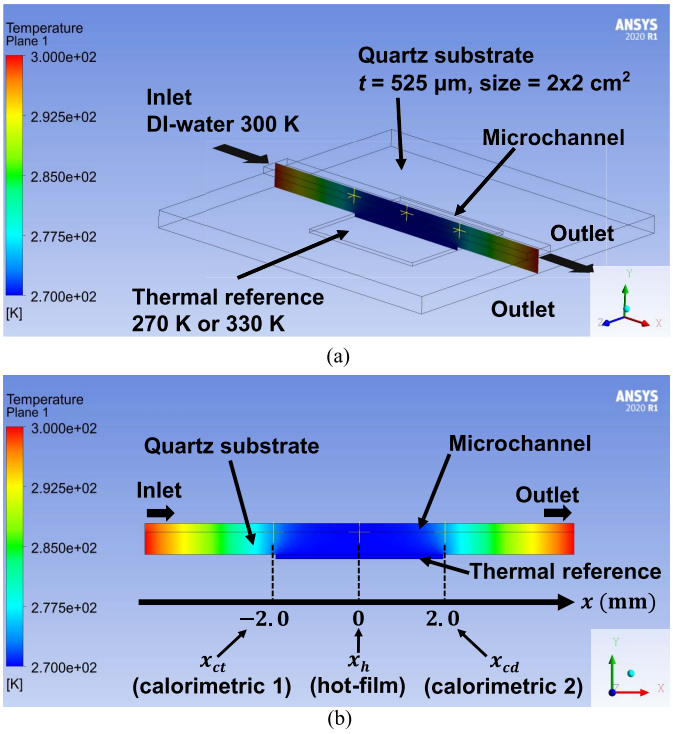

Fig. 2. (a) Model used for CFD simulation. (b) Cross-sectional view of the CFD simulation, where the temperature difference ($\Delta T_{\mathrm{Peltier}}$) was set to −30°C at the thermal reference block. We measured the temperature at x_{ct}, x_{h}, and x_{cd} for each flow rate and calculated the temperature changes ($\Delta T_{\mathrm{c}} = \Delta T_{\mathrm{cd}} - \Delta T_{\mathrm{ct}}$ and ΔT_{h}).

hot-film sensor measures the resistive change of R_{h} using a constant current source (I), and the output voltage (V_{h}) is then expressed as

$$\Delta V_h = \alpha G R_{h0} I \Delta T_h(u), \tag{2}$$

where G is the gain of the amplifier and ΔT_{h} is the temperature change. In contrast, in the high-resolution calorimetric sensor, the Wheatstone bridge output using R_{ct} and R_{cd} is amplified and monitored, as shown in Fig. 1(b). The output voltage (V_{c}) is expressed as

$$\Delta V_c = \frac{1}{4}\alpha V_B G \Delta T_c(u), \tag{3}$$

where V_{B} is the voltage applied to the Wheatstone bridge and ΔT_{c} is the temperature difference between R_{ct} and R_{cd}.

III. FEM Simulation

Before measuring the fabricated sensor, we investigated the temperature changes in the microchannel using CFD simulations. We used ANSYS Fluent as the CFD simulator. To simplify the model, we modeled a thermal referential rectangular block at the center of the quartz substrate, as shown in Fig. 2. The block size was 3.96 × 3.96 mm^2, which was the same dimension as that of the Peltier module used in the experiment. Using the rectangular block, we applied a temperature difference ($\Delta T_{\mathrm{Peltier}}$) from the backside of the quartz substrate. We input water flow at 27°C and increased the flow rate (u) from 10 nL/min to 200 μL/min. We then measured the temperature changes (ΔT_{ct}, ΔT_{h}, and ΔT_{cd})

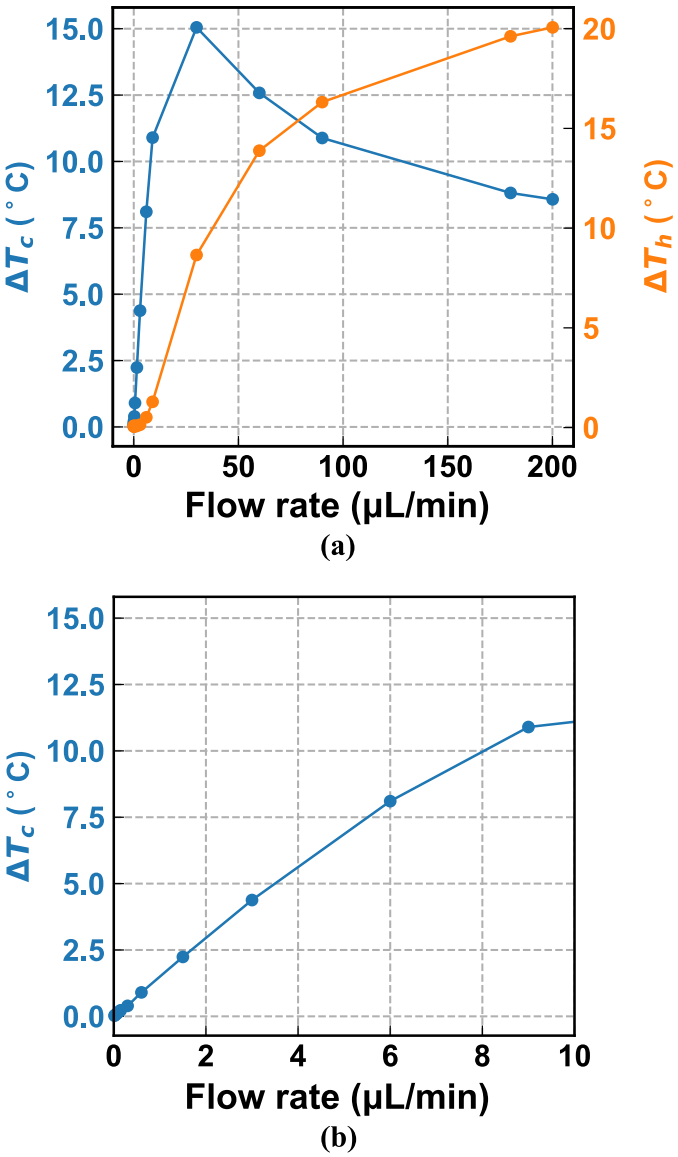

Fig. 3. (a) CFD simulation results of the temperature changes in calorimetric and hot-film sensors (ΔT_c and ΔT_h) in the cooling mode, where the temperature difference was set to -30°C. (b) Closed-up of results of the temperature changes of the calorimetric thermal flow sensor (ΔT_c) in the low flow rate region (<10 μL/min).

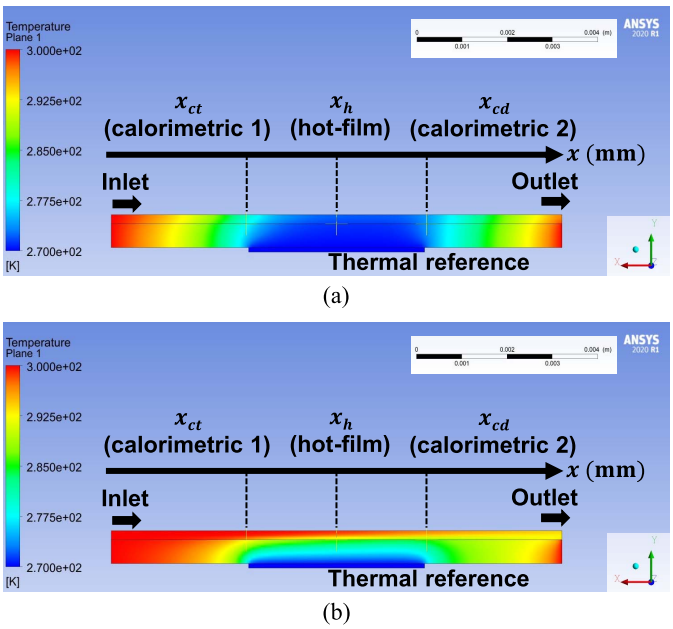

Fig. 4. CFD simulation results in the cooling mode, where the temperature difference is -30°C and the flow rate is (a) 3 μL/min and (b) 200 μL/min.

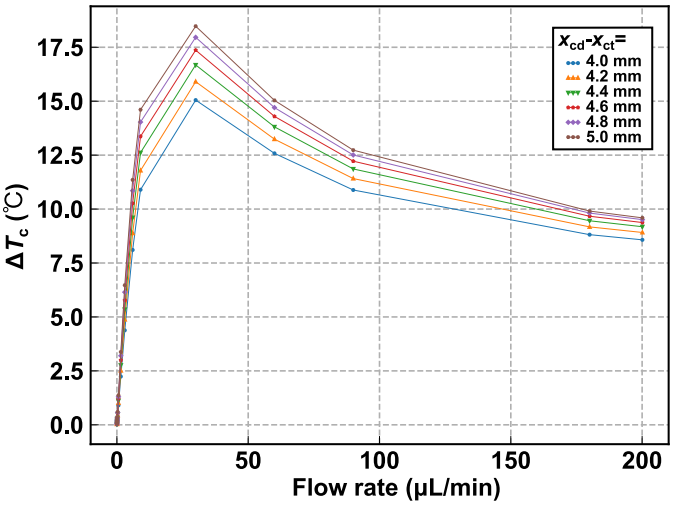

Fig. 5. CFD simulation results of a calorimetric sensor for different distances ($x_{cd} - c_{ct}$), where $\Delta T_{Peltier}$ is -30°C.

at the thermal sensor locations (x_{ct}, x_h, and x_{cd}) as shown in Figure 2(b). We set $\Delta T_{Peltier}$ to -30°C for cooling-mode simulation and 30°C for heating-mode simulation.

Figures 3(a) and 3(b) show the temperature changes of the calorimetric ($\Delta T_c = \Delta T_{cd} - \Delta T_{ct}$) and hot-film ($\Delta T_h$) sensors in the cooling mode when the input water flow rate (u) was changed. As shown in Fig. 3, the calorimetric sensor measured the flow at a low flow rate. However, as the flow rate increased, ΔT_c decreased. This curve shape is common for calorimetric sensors. The signal decreases on both thermo-resistive sensors owing to heavy convective cooling [9], [22]. To investigate this phenomenon, we compared the thermal distribution at low and high flow rates. Figures 4(a) and 4(b) show the temperature distributions when the flow rate is 3 μL/min and 200 μL/min, respectively. As shown in Figs. 4(b), the thermal distribution generated by the thermal reference does not change according to Fig. 1, when the flow rate is high. Conversely, the hot-film sensor can measure high flow rates, while it hardly shows a response to low flow rates. Figure 3(b) shows the response of ΔT_c in the low flow rate region (< 10 μL/min). These results indicate that the calorimetric sensor can measure low flow rates with high resolution. Therefore, wide flow rate ranges can be measured using both the calorimetric and hot-film sensors.

Figure 5 shows the simulation results of the calorimetric sensor for different distances between x_{ct} and x_{cd} ($= x_{cd} - x_{ct}$), where the $\Delta T_{Peltier}$ is set to -30°C. In this simulation, the distance ($x_{cd} - x_{ct}$) is changed from 4.0 mm to 5.0 mm with a step size of 0.2 mm. As shown in Fig. 5, the temperature change increases as the distance ($x_{cd} - x_{ct}$) increases. Next, we simulated the sensitivity dependence of ΔT_c on $\Delta T_{Peltier}$. Figure 6(a) shows ΔT_c when $\Delta T_{Peltier}$ is set to -30°C and -10°C. Although the magnitude of ΔT_c depends on

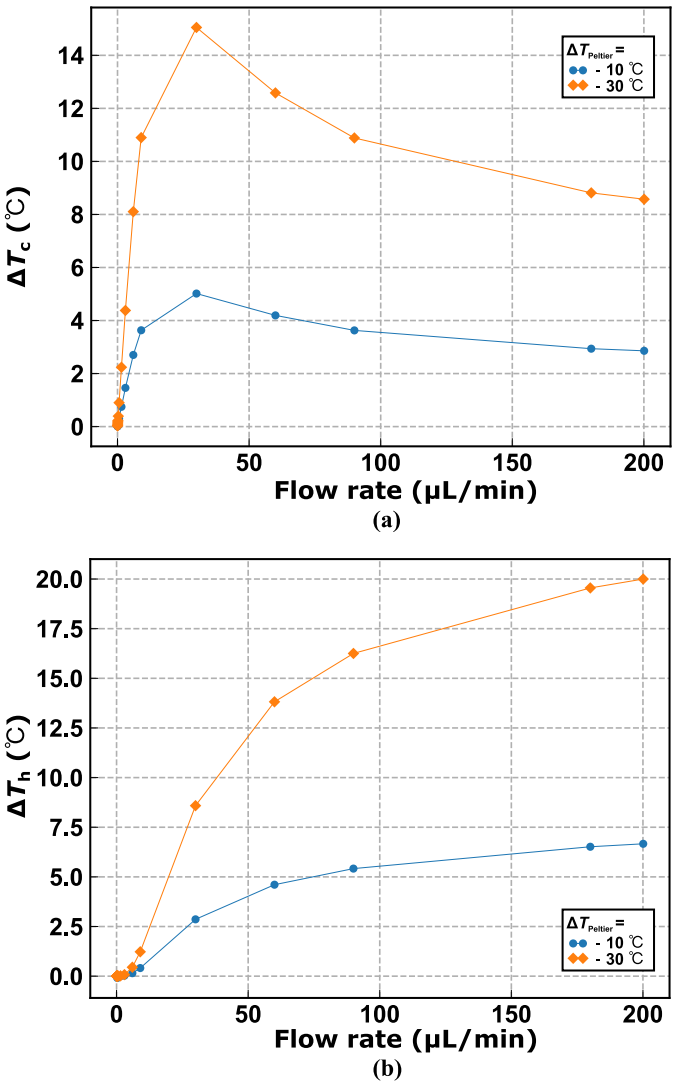

Fig. 6. CFD simulation results of (a) calorimetric and (b) hot-film sensors for different $\Delta T_{\text{Peltier}}$ values, where the distance between the two sensors in the calorimetric sensor ($x_{\text{cd}} - c_{\text{ct}}$) is 4.0 mm.

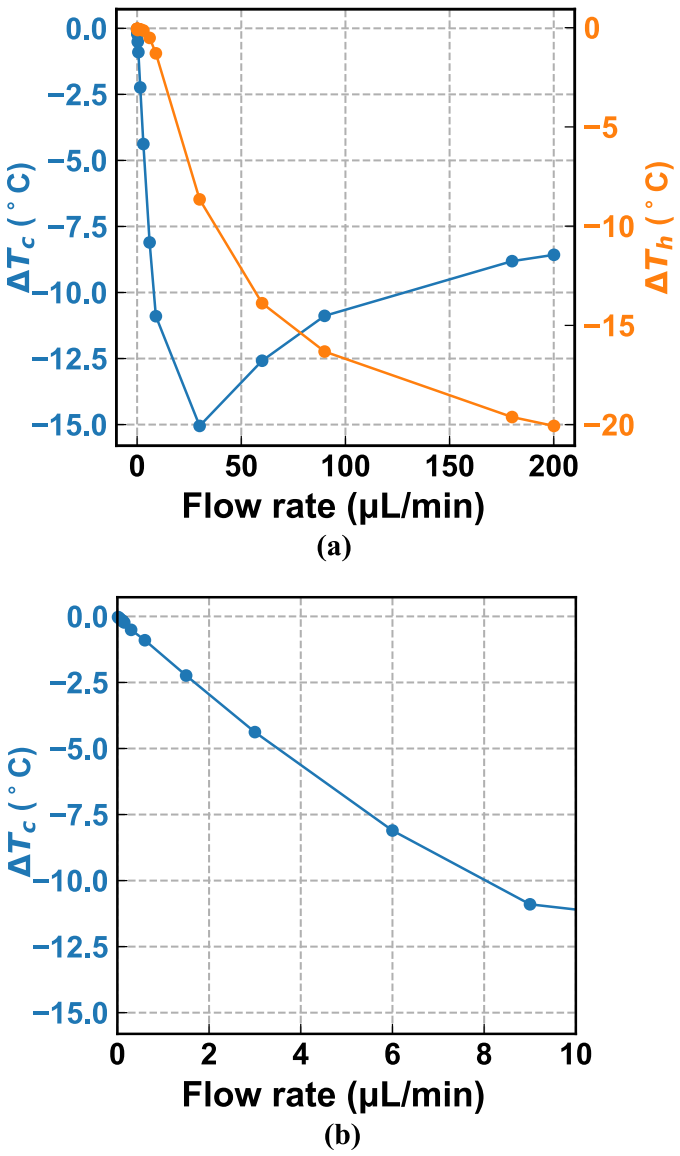

Fig. 7. (a) CFD simulation results of the temperature changes in calorimetric and hot-film sensors (ΔT_{c} and ΔT_{h}) in the heating mode, where the temperature difference was set to 30°C. (b) Zoomed-in plot of results of the temperature changes of the calorimetric thermal flow sensor (ΔT_{c}) in the low flow rate region (<10 μL/min).

$\Delta T_{\text{Peltier}}$, the trend of ΔT_c for each condition of $\Delta T_{\text{Peltier}}$ is similar. Figure 6(b) shows ΔT_{h} when $\Delta T_{\text{Peltier}}$ is set to -30°C and -10°C. In the case of ΔT_{h} and ΔT_{c}, the trend of ΔT_c is similar at $T_{\text{Peltier}} = -10$°C and $T_{\text{Peltier}} = -30$°C.

Figures 7(a) and 7(b) show the simulation results of the heating mode. In the heating mode, the temperature changes were inverted. Similar to the cooling mode, the calorimetric sensor responded sensitively at low flow rates and the hot-film sensor responded at high flow rates in the heating mode. Figure 7(b) shows the response of ΔT_{c} in the low flow rate region ($<$ 10 μL/min). Therefore, the simulation results indicate that the proposed sensor can be used in both cooling and heating modes.

IV. Fabrication

Figure 8 illustrates the fabrication process of the proposed device. We used a 525-μm-thick quartz wafer. First, 20-nm-thick titanium, 200-μm-thick gold, and 20-nm-thick titanium were sputtered (Fig. 8(a)) at 25°C, where the last titanium layer was adhered to SU-8 [23], [24]. The positive photoresist (JSR 7790G, JSR) was then patterned, and the titanium and gold layers were then etched using 5% APM and gold etchant (AURUM-302, KANTO CHEMICAL), respectively (Fig. 8(b)). After removing the photoresist using acetone, the 5-μm-thick permanent negative photoresist SU-8 3005 was patterned as an isolating layer (Fig. 8(c)). As the SU-8 is a widely-used insulating permanent material in microfluidic applications [13], [23]–[27], we chose this material as an isolating material between the fluid and electrodes. Subsequently, the quartz wafer was dipped into (3-aminopropyl)triethoxysilane (APTES) and rinsed with deionized (DI) water to create amine groups on the surface (Fig. 8(d)). Surface modification with APTES enables bonding between SU-8 and PDMS [25]. Next, poly-dimethylsiloxane (PDMS) was patterned using a silicon mold (Fig. 8(e)). The

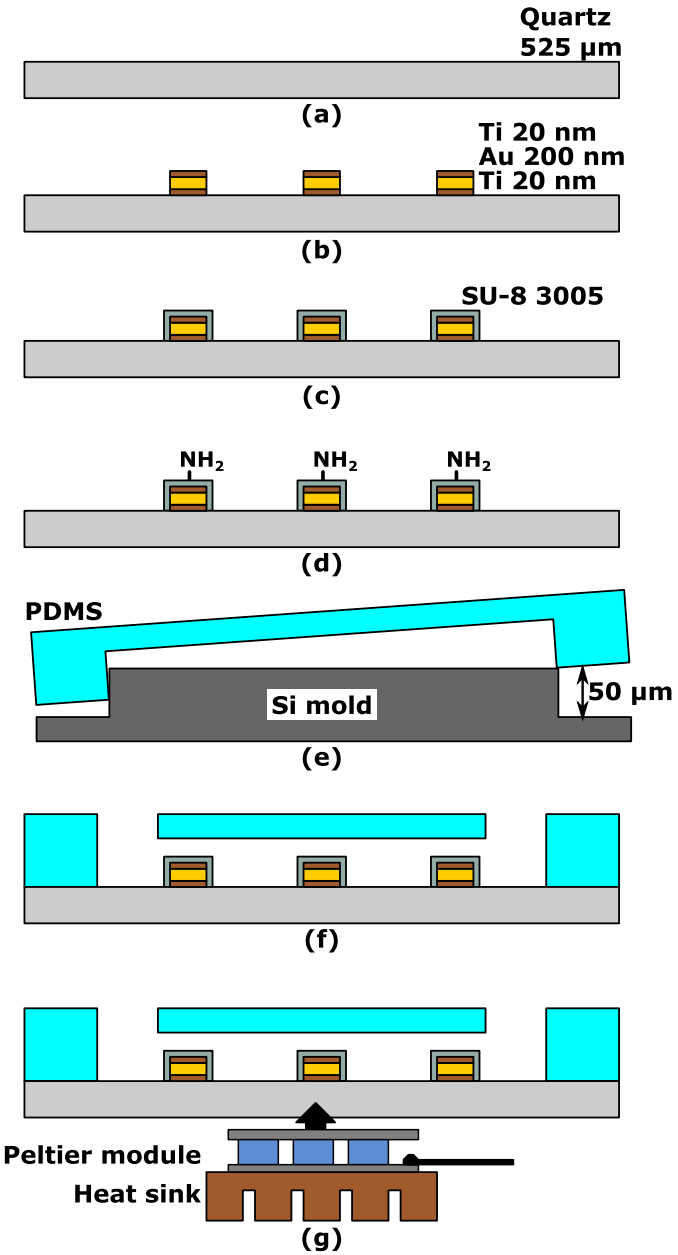

Fig. 8. Process flow of the proposed device. (a) Ti, Au, and Ti are sputtered sequentially on a quartz wafer. (b) Each metal layer is wet-etched. (c) SU-8 isolating layer is patterned. (d) Amine groups are created on the surface using APTES. (e) PDMS is patterned using a silicon mold. (f) The PDMS substrate is bonded on the quartz chip using O_2 plasma. (g) A Peltier module and a heat sink are attached.

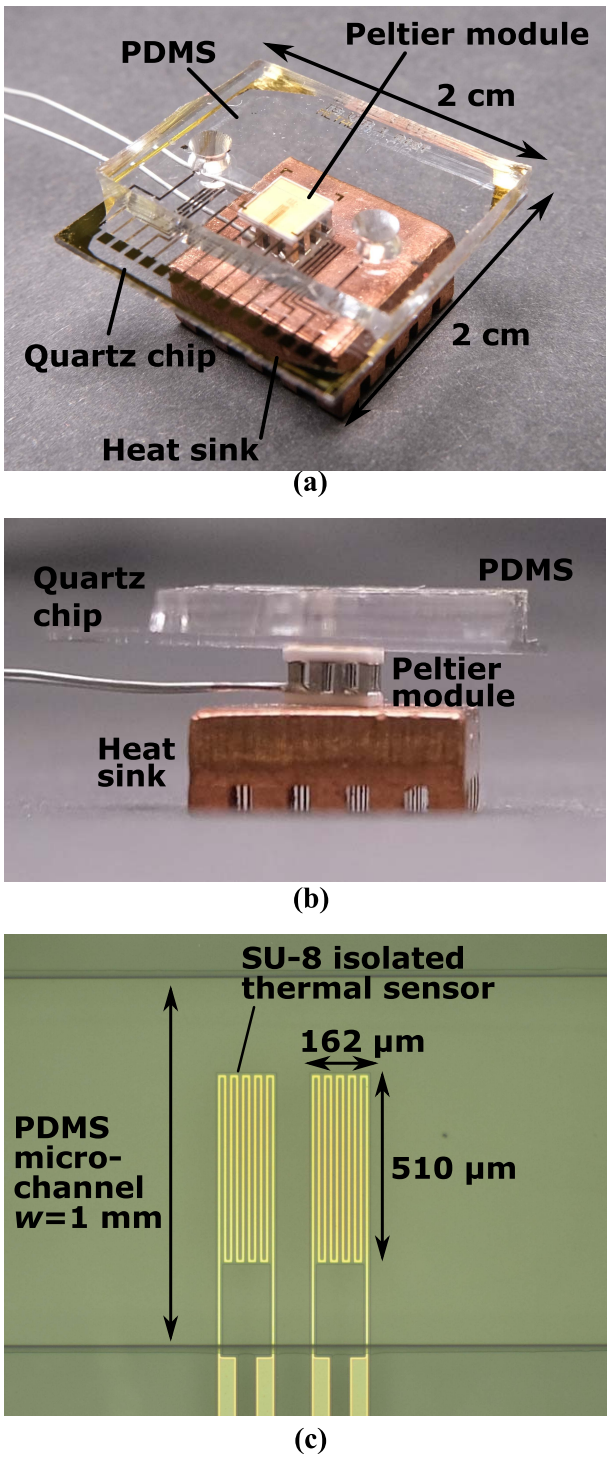

Fig. 9. (a) Image of the fabricated cooling thermal flow sensor chip. (b) Cross-sectional view of the fabricated chip. (c) Zoomed-in photomicrograph of the thermo-resistive sensor. Both calorimetric and hot-film sensors use the same design.

mold was patterned using DRIE and was fluorinated with a mold-release coating agent (SURECO 2101S, AGC). The inlet and outlet holes were punched into the PDMS, which was bonded to the quartz chip using O_2 plasma activation (Fig. 8(f)). The O_2 plasma activates both quartz and PDMS surface. Finally, a $3.96 \times 3.96 \times 2.4\text{mm}^3$ Peltier module (NL1010T, Marlow Industries, Inc.) and copper heat sink were attached to the chip (Fig. 8(g)). Figure 9(a) shows the fabricated thermal flow sensor and Fig. 9(b) shows the cross-sectional view of the sensor chip stacked with the Peltier module and heat sink. The size of the chip was 2×2 cm^2. The PDMS microchannel's length, width, and thickness were 10 mm, 1000 μm, and 50 μm, respectively. Figure 9(c) shows a zoomed-in photomicrograph of a thermo-resistive sensor integrated into the microchannel. One of the two thermo-resistive sensors was a spare in case the other broke, and only one of them was used during the experiment. We placed two sensors at the calorimetric sensor location (R_{ct}, R_{cd}) and three thermo-resistive sensors at the hot-film

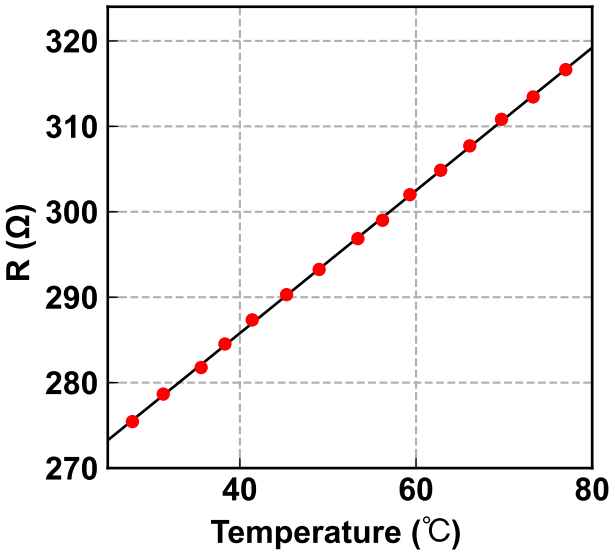

Fig. 10. Temperature coefficient of resistance (TCR) of the thermo-resistive sensor used in the calorimetric and hot-film sensors.

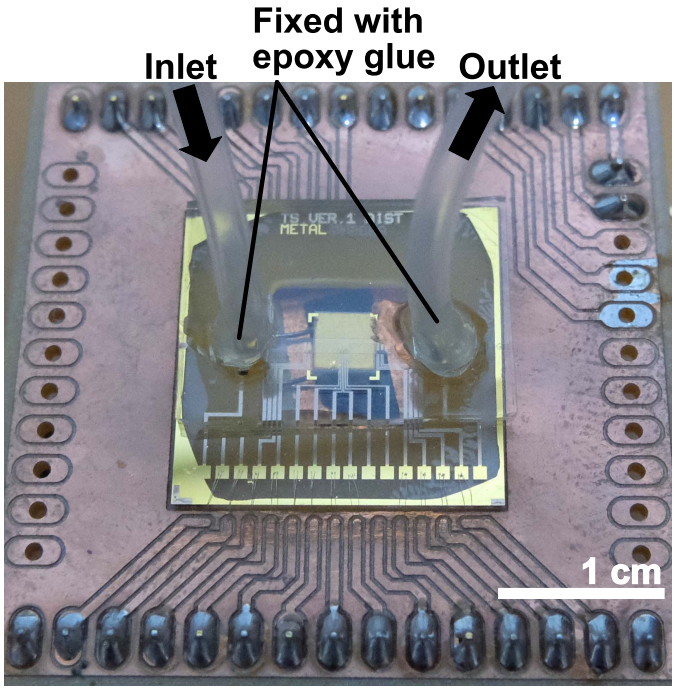

Fig. 11. Image of the fabricated cooling thermal flow sensor chip connected with inlet and outlet silicone tubes using silicone glue. The chip is attached to a PCB and is wire-bonded.

sensor location (R_h) as spares. The calorimetric sensors were located at ±2.10 mm from the center (i.e., $x_{ct} = -2.10$ mm and $x_{cd} = 2.10$ mm). The hot-film sensor was placed at the center (i.e., $x_h = 0$mm).

V. Measurement and Results

We used the same design of a thermo-resistive sensor for both calorimetric and hot-film sensors. Before the flow measurement, we measured the thermal coefficient of resistance (TCR) of the thermo-resistive sensor. We placed the sensor chip on a hot plate and measured the chip temperature and the sensor resistance using a thermometer (SN3000,

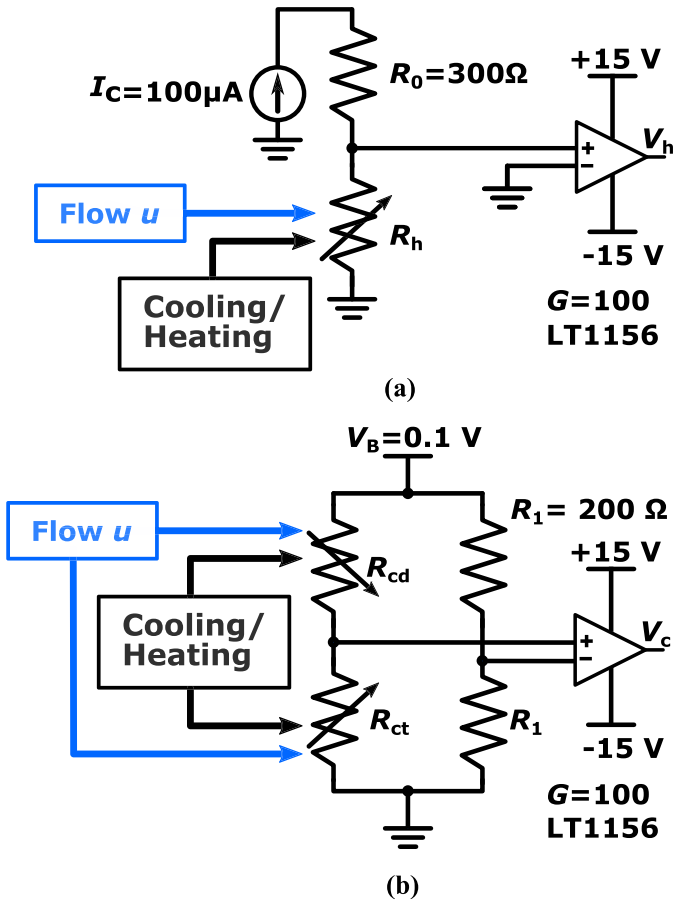

Fig. 12. (a) Measurement circuit of a wide-range hot-film flow sensor. (b) Measurement circuit of the high-resolution calorimetric sensor.

NETSUKEN) and an LCR meter (IM3536, HIOKI), respectively. The sensing probe of the thermometer was placed in contact with the quartz substrate of the sensor chip. Figure 10 shows the TCR of the sensor measured between 27.8°C and 77.0°C. Although we measured the TCR only when the temperature was higher than the 25°C owing to the limitations of the equipment, we considered the resistance to be proportional to temperature in both the cooling and heating modes based on our experimental results.

An experiment on the fabricated device was performed using DI water. The flow rate was controlled by a programmable syringe pump (Legato 110, KD Scientific) connected to a sensor with silicone tubes. Figure 11 shows the fabricated device attached to a printed circuit board (PCB), where the Peltier module is located from the backside of the device through a rectangular hole in the PCB. We applied 44 mW to the Peltier module in cooling mode in the forward direction. In the heating mode, we applied the same power of 44 mW in the reverse direction. Figures 12(a) and 12(b) show the measurement circuit containing the calorimetric and hot-film thermal sensors. As shown in Fig. 12(a), we set the current (I_c) to 100 μA in the hot-film sensor using a power source (B2962A, Keysight). As the power consumption at the hot-film sensor is less than 50 μW, the current was sufficiently low to ignore the self-heating effect of the thermo-resistive sensors. As shown in Fig. 12(b), the applied voltage to the

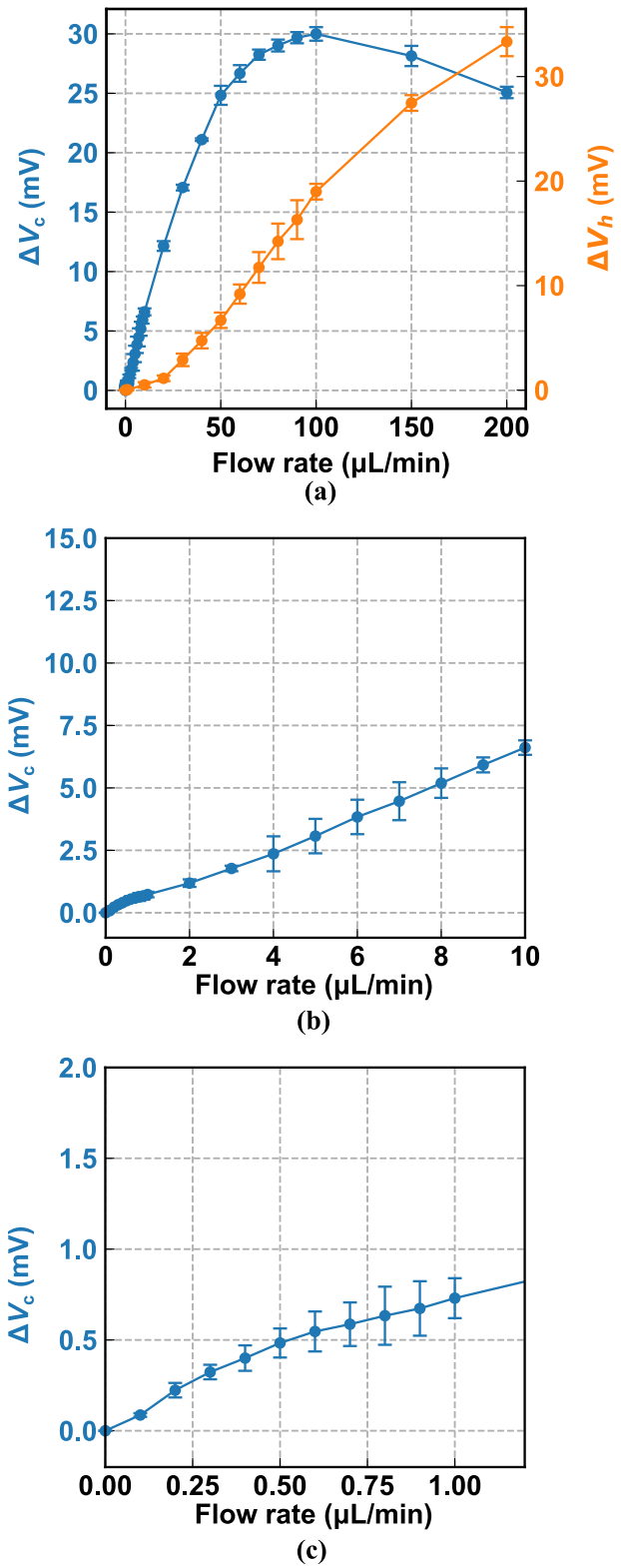

Fig. 13. (a) Measurement results of the output voltage of the calorimetric (V_c) and hot-film thermal flow sensors (V_h) in the cooling mode. The gain of the amplifier G is set to 100 in both sensors. The applied voltage to the Wheatstone's bridge in the calorimetric sensor (V_B) is 0.1 V. The current for the hot-film sensor (I_C) is set to 100 μ A. (b) and (c) Measurement results of the output voltage of the calorimetric thermal flow sensor (V_c) in the low flow rate region (<10 μL/min and <1 μL/min).

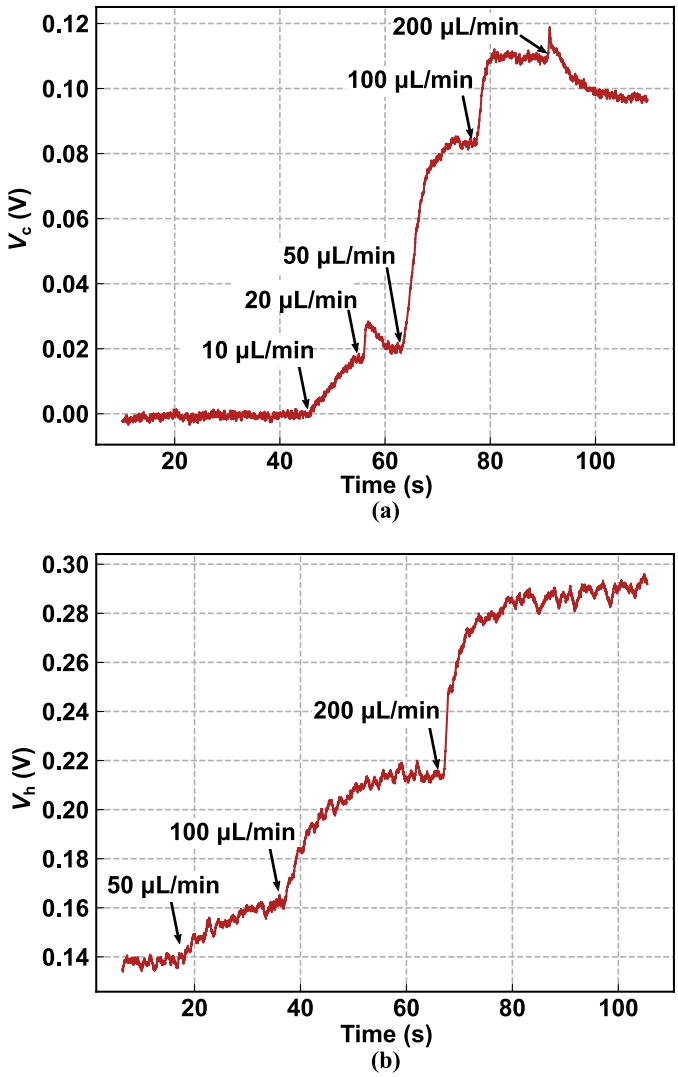

Fig. 14. Transient output of (a) the calorimetric sensor and (b) the hot-film sensor in the cooling mode when the flow rate is changed.

Wheatstone's bridge (V_B) was set to 0.1 V using a source meter (2460, Keithley) in the calorimetric sensor. To amplify the signals, we used an instrumentation amplifier (LT1167, Analog Devices) and set the gain (G) to 100 for both the calorimetric and hot-film sensors.

Figure 13(a) shows the experimental results for hot-film and calorimetric sensor output voltages (V_c and V_h) in the cooling mode. Figures 13(b) and 13(c) show the calorimetric sensor voltage output in the low flow rate region. As expected from the preliminary simulation shown in Fig. 3, V_h indicates that the hot-film sensor has a low response when the flow rate is low. The responses of the hot-film sensor corresponded to the simulation results as the flow rate increased. The hot-film sensor could measure higher flow rates, unlike the calorimetric sensor, whose response decreased when the flow rate was higher than 100 μL/min.

In contrast, V_c indicates that the calorimetric sensor measures low-resolution flow rates (less than 10 μL/min). Figure 13(b) shows the output of the calorimetric sensor (V_c) when the flow rate is less than 10 μL/min, and Fig. 13(c) shows V_c when the flow rate is less than 1 μL/min. The minimum flow rate in the experiment was 100 nL/min because of limitations associated with the syringe pump. As shown in

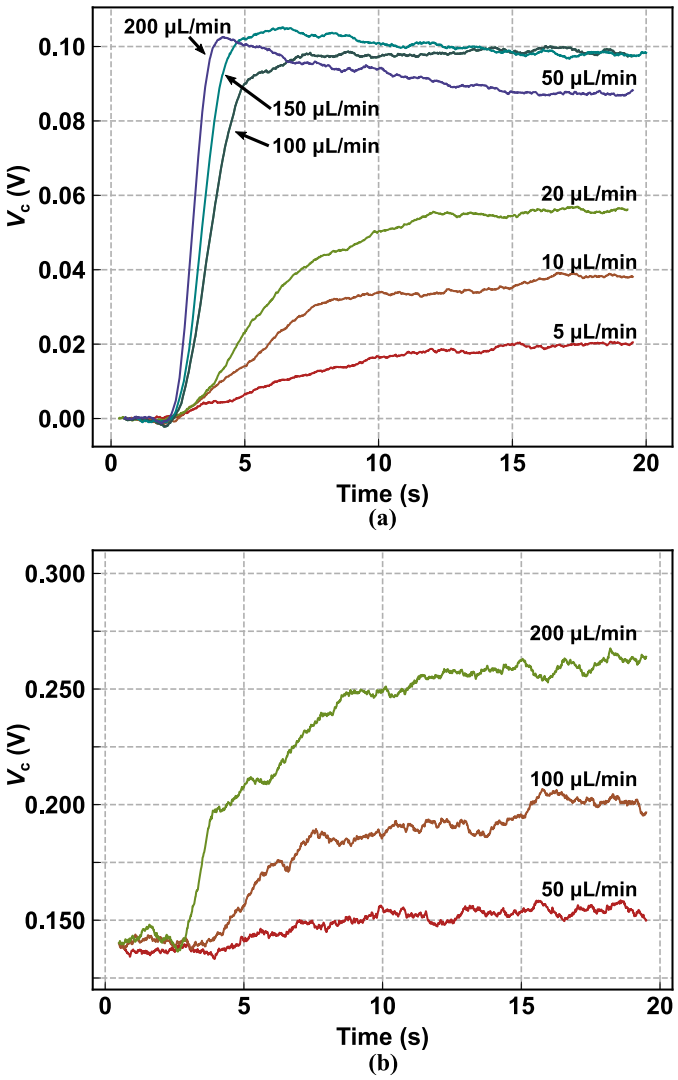

Fig. 15. Transient responses of (a) the calorimetric sensor and (b) the hot-film sensor in the cooling mode when the pump was turned on with different flow rates.

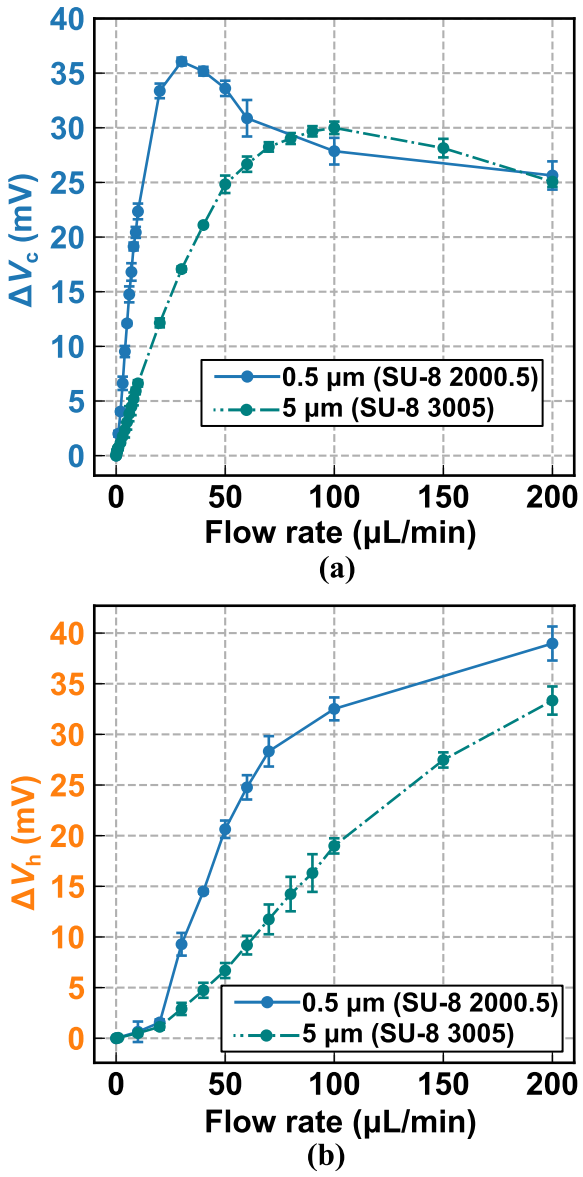

Fig. 16. Output of (a) the calorimetric sensor and (b) the hot-film sensor with 0.5-μm-thick and 5-μm-thick SU-8 insulating layers.

Fig. 13(b), V_c successfully detected these flow rates linearly in the low flow-rate region.

Figures 14(a) and 14(b) show the oscilloscope (DSOX1204G, Keysight) measurement results of the outputs of the cooling-mode calorimetric and hot-film sensors with varying time, where the same power (44 mW) was applied to the Peltier module. because of the minimum resolution of the oscilloscope, we increased the gain of the measurement circuit (G) to 500. During the measurement, we changed the flow rates and measured V_c and V_h. As shown in Fig 14(a), V_c increased as the flow rate increased. However, when the flow rate became 200 μL/min, V_c decreased. The results corresponded to the static measurement shown in Fig. 13. As shown in Fig. 14(b), V_h increases when the flow rate increases. As with the static analysis results shown in Fig. 13, V_h increases monotonically, even when the flow rate is high.

Figure 15 show the transient responses when the pump is turned on with different flow rates in the calorimetric and hot-film sensors. As shown in Fig. 15(a), the rising time becomes shorter when the flow rate increases in the calorimetric sensor. In the hot-film mode also, the rising time becomes shorter when the flow rate increases, as shown in Fig. 15(b). Compared to the calorimetric sensor, longer rising time was required in the hot-film sensor. This is because the differential measurement used in the calorimetric sensor reduces the drift [28].

As shown in Fig. 13, V_c starts to drop at 100 μL/min. It occurs at a higher flow rate than the simulating results, as shown in Fig. 3. We consider that the SU-8 insulating layer increases the measurement range by moderating the temperature change. To investigate the effect of SU-8 insulating layer thickness, we fabricated the sensor device with thinner insulating SU-8 layer using SU-8 2000.5. The thickness of SU-8 2000.5 was 0.5 μm, and we compared the outputs of the calorimetric and hot-film sensors with 0.5-μm-thick and 5-μm-thick device. Figure 16 show the result of the calorimetric and hot-film sensors for different SU-8 insulating layer thicknesses. As shown in Figs. 16(a) and 16(b),

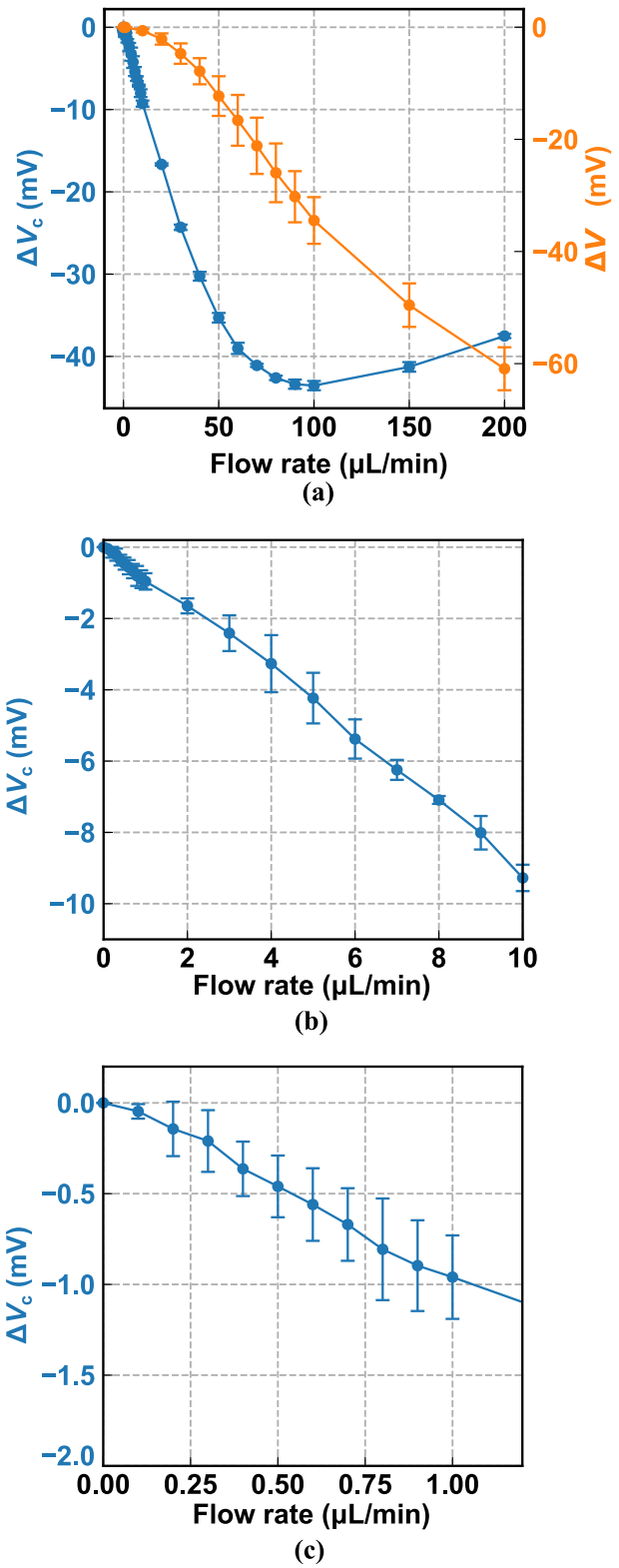

Fig. 17. (a) Measurement results of the output voltage of calorimetric (V_c) and hot-film thermal flow sensors (V_h) in the heating mode. The gain of the amplifier G is set to 100 in both sensors. The applied voltage to the Wheatstone's bridge in the calorimetric sensor (V_B) is 0.1 V. The current for the hot-film sensor (I_C) is set to 100 μ A. (b) and (c) Measurement results of the output voltage of the calorimetric thermal flow sensor (V_c) in the low flow rate region (<10 μL/min and <1 μL/min).

in the 0.5-μm-thick SU-8 device, the output voltages were relatively higher than the 5-μm-thick SU-8 device. On the other hand, the decrease occurred at the lower flow rate in the 0.5-μm-thick SU-8 device compared to the 5-μm-thick SU-8 device. The shape of the output of the 0.5-μm-thick SU-8 device is similar to the simulation results, which did not contain the insulating layer effect. Therefore, we can infer that the change of the maximum-output flow rate is caused by the SU-8 layer, and reducing the thickness of the SU-8 layer increases the sensitivity of the sensor. However, the 0.5-μm-thick SU-8 layer was easily stripped when the flow rate was quite high (> 200 μL/min). When the SU-8 layer was damaged, bubbles were generated around the electrodes. Therefore, an SU-8 layer thick enough to protect the electrodes is required, although this reduces the sensitivity.

Figures 17(a), 17(b) and 17(c) show the experimental results in the heating mode. Similar to the cooling mode, the calorimetric sensor responded sensitively at low flow rates, and the hot-film sensor responded at high flow rates (up to 200 μL/min). Figures 17(b) and 17(c) show the output of the calorimetric sensor (V_c) when the flow rate was less than 10 μL/min and 1 μL/min, respectively. Therefore, the measurement results were representative of the simulation in the cooling and heating modes, indicating that the sensor can be used in both modes.

VI. Conclusion

In this study, we propose a thermal flow sensor with bidirectional thermal reference. The thermal reference generates cooling and heating thermal distributions depending on the flow rate. We fabricated integrated calorimetric and hot-film thermal flow sensors using a Peltier module as a bidirectional thermal reference, which created a thermal distribution. The proposed sensor expands the use of the thermal flow sensors by switching between the cooling and heating modes according to the sample temperature and maximum temperature limit. In the cooling mode, the proposed sensor can monitor the flow rate in a microfluidic device without heating the reagent.

Additionally, the proposed sensor can be used as a conventional heating thermal flow sensor by inverting the current direction. We demonstrated the proposed thermal flow sensor using CFD simulation and experimental results in both heating and cooling modes. The calorimetric sensor can measure low flow rates with 100 nL/min resolution, whereas the hot-film sensor can measure a wide range of flow rates up to 200 μL/min. The sensor will help reduce the amount of reagents used in LOC and μTAS applications, including temperature-limited applications.

Acknowledgment

The patterning of the device was carried out using open facilities maintained by the Nanotechnology Platform Program of MEXT and The University of Tokyo, and the photomask was fabricated using the System Design Laboratory. (d. lab) 8-inch EB writer F5112+VD01 donated by Advantest Corporation.

References

[1] D. Liu, H. Zhang, F. Fontana, J. T. Hirvonen, and H. A. Santos, "Current developments and applications of microfluidic technology toward clinical translation of nanomedicines," *Adv. Drug Del. Rev.*, vol. 128, pp. 54–83, Mar. 2018.

[2] E. Verpoorte and N. F. De Rooij, "Microfluidics meets MEMS," *Proc. IEEE*, vol. 91, no. 6, pp. 930–953, Jun. 2003.
[3] C. Zhao and C. Yang, "Advances in electrokinetics and their applications in micro/nano fluidics," *Microfluidics Nanofluidics*, vol. 13, no. 2, pp. 179–203, Sep. 2012.
[4] P.-W. Yen *et al.*, "A low-power CMOS microfluidic pump based on travelling-wave electroosmosis for diluted serum pumping," *Sci. Rep.*, vol. 9, no. 1, pp. 1–8, Oct. 2019.
[5] Y. Okamoto, H. Ryoson, K. Fujimoto, T. Ohba, and Y. Mita, "On-chip CMOS-MEMS-based electroosmotic flow micropump integrated with high-voltage generator," *J. Microelectromech. Syst.*, vol. 29, no. 1, pp. 86–94, Feb. 2020.
[6] Y. Okamoto, H. Takehara, K. Fujimoto, T. Ichiki, T. Ohba, and Y. Mita, "On-chip high-voltage charge pump with MEMS post-processed standard 5-V CMOS on SOI for electroosmotic flow micropumps," *IEEE Electron Device Lett.*, vol. 39, no. 6, pp. 851–854, Jun. 2018.
[7] W. Xu *et al.*, "A wireless dual-mode micro thermal flow sensor system with extended flow range by using CMOS-MEMS process," in *Proc. IEEE Micro Electro Mech. Syst. (MEMS)*, Jan. 2018, pp. 824–827.
[8] W. Xu, X. Wang, R. W. Izhar, J. Xu, and Y.-K. Lee, "CMOS MEMS thermal flow sensor with enhanced sensitivity for heating, ventilation, and air conditioning application," *IEEE Trans. Ind. Electron.*, vol. 68, no. 5, pp. 4468–4476, May 2021.
[9] E. Meng, P.-Y. Li, and Y.-C. Tai, "A biocompatible Parylene thermal flow sensing array," *Sens. Actuators A, Phys.*, vol. 144, no. 1, pp. 18–28, May 2008.
[10] S.-I. Ohira and K. Toda, "Miniature liquid flow sensor and feedback control of electroosmotic and pneumatic flows for a micro gas analysis system," *Anal. Sci.*, vol. 22, no. 1, pp. 61–65, Jan. 2006.
[11] I. Etchart *et al.*, "MEMS sensors for density–viscosity sensing in a low-flow microfluidic environment," *Sens. Actuators A, Phys.*, vol. 141, no. 2, pp. 266–275, Feb. 2008.
[12] Y. Okamoto, H. Ryoson, K. Fujimoto, K. Honjo, T. Ohba, and Y. Mita, "Hotspot liquid microfluidic cooling: Comparing the efficiency between horizontal flow and vertical flow," *J. Phys., Conf.*, vol. 773, Nov. 2016, Art. no. 012066.
[13] Y. Okamoto, K. Fujimoto, H. Ryoson, T. Ohba, and Y. Mita, "Stick-to-analyze zeta potential measurement chip with integrated electroosmotic micropump and liquid flow sensor," in *Proc. IEEE 32nd Int. Conf. Micro Electro Mech. Syst. (MEMS)*, Jan. 2019, pp. 437–440.
[14] F. Ejeian *et al.*, "Design and applications of MEMS flow sensors: A review," *Sens. Actuators A, Phys.*, vol. 295, pp. 483–502, Aug. 2019.
[15] V. Balakrishnan, T. Dinh, H.-P. Phan, D. V. Dao, and N.-T. Nguyen, "Highly sensitive 3C-SiC on glass based thermal flow sensor realized using MEMS technology," *Sens. Actuators A, Phys.*, vol. 279, pp. 293–305, Aug. 2018.
[16] W. Iwasaki, H. Nogami, S. Takeuchi, M. Furue, E. Higurashi, and R. Sawada, "Detection of site-specific blood flow variation in humans during running by a wearable laser Doppler flowmeter," *Sensors*, vol. 15, no. 10, pp. 25507–25519, Oct. 2015.
[17] A. G. P. Kottapalli, C. W. Tan, M. Olfatnia, J. M. Miao, G. Barbastathis, and M. Triantafyllou, "A liquid crystal polymer membrane MEMS sensor for flow rate and flow direction sensing applications," *J. Micromech. Microeng.*, vol. 21, no. 8, Jun. 2011, Art. no. 085006.
[18] A. F. P. Van Putten and S. Middelhoek, "Integrated silicon anemometer," *Electron. Lett.*, vol. 10, no. 21, pp. 425–426, Oct. 1974.
[19] N. T. Nguyen, "Micromachined flow sensors—A review," *Flow Meas. Instrum.*, vol. 8, no. 1, pp. 7–16, Mar. 1997.
[20] A. R. Moritz and F. C. Henriques, Jr., "Studies of thermal injury: II. The relative importance of time and surface temperature in the causation of cutaneous burns," *Amer. J. Pathol.*, vol. 23, no. 5, pp. 695–720, Sep. 1947.
[21] Y. Okamoto, T.-V. Nguyen, H. Okada, and M. Ichiki, "On-chip cooling thermal flow sensor for biological applications," in *Proc. IEEE 34th Int. Conf. Micro Electro Mech. Syst. (MEMS)*, Jan. 2021, pp. 756–759.
[22] N. T. Nguyen and W. Dötzel, "Asymmetrical locations of heaters and sensors relative to each other using heater arrays: A novel method for designing multi-range electrocaloric mass-flow sensors," *Sens. Actuators A, Phys.*, vol. 62, nos. 1–3, pp. 506–512, Jul. 1997.
[23] Y. Okamoto *et al.*, "Z-axis controllable mille-feuille electrode electrorotation device utilizing levitation effect," in *Proc. 20th Int. Conf. Solid-State Sensors, Actuat. Microsyst. Eurosensors (TRANSDUCERS EUROSENSORS)*, Jun. 2019, pp. 213–216.
[24] T. Tsuchiya *et al.*, "Two-dimensionally arrayed double-layer electrode device which enables reliable and high-thoroughput electrortation," in *Proc. IEEE 34th Int. Conf. Micro Electro Mech. Syst. (MEMS)*, Jan. 2021, pp. 486–489.
[25] Y. Ren *et al.*, "A simple and reliable PDMS and SU-8 irreversible bonding method and its application on a microfluidic-MEA device for neuroscience research," *Micromachines*, vol. 6, no. 12, pp. 1923–1934, Dec. 2015.
[26] J. Carlier *et al.*, "Integrated microfluidics based on multi-layered SU-8 for mass spectrometry analysis," *J. Micromech. Microeng.*, vol. 14, pp. 619–624, Feb. 2004.
[27] K. P. Nichols, J. C. T. Eijkel, and H. J. G. E. Gardeniers, "Nanochannels in SU-8 with floor and ceiling metal electrodes and integrated microchannels," *Lab Chip*, vol. 8, no. 1, pp. 173–175, Jan. 2008.
[28] T. Q. Hudson and E. Meng, "A continuous, impedimetric parylene flow sensor," *J. Microelectromech. Syst.*, vol. 30, no. 3, pp. 456–470, Jun. 2021.

Yuki Okamoto (Member, IEEE) received the B.E., M.E., and Ph.D. degrees in electrical engineering from The University of Tokyo, Japan, in 2015, 2017, and 2020, respectively. He is currently a Researcher at the Sensing System Research Center (SSRC), National Institute of Advanced Industrial Science and Technology (AIST), Tsukuba, Japan. His research interests include CMOS-MEMS sensors and actuators, particularly free-space optical devices, such as MEMS scanners for light detection and ranging (LiDAR) and integrated microfluidics for lab-on-a-chip and μTAS applications.

Thanh-Vinh Nguyen received the B.E., M.E., and Ph.D. degrees in mechano-informatics from The University of Tokyo, Japan, in 2010, 2012, and 2015, respectively. He is currently a Researcher at the Sensing System Research Center (SSRC), National Institute of Advanced Industrial Science and Technology (AIST), Tsukuba, Japan. His research interests include MEMS-based force sensors, acoustic sensors, droplet dynamics, and wearable health monitoring devices.

Hironao Okada received the B.E. degree in materials science and engineering from Kyoto University in 2001 and the M.E. and Ph.D. degrees in precision engineering from The University of Tokyo in 2003 and 2007, respectively. After working as a Researcher at The University of Tokyo for one year, he became a Researcher at the National Institute of Advanced Industrial Science and Technology (AIST) in 2008. He is currently a Senior Researcher at the Sensing System Research Center, AIST. His research interests include wireless sensor network systems, low-power wireless communication technology, and electrochemical sensors for monitoring biological information.

Masaaki Ichiki received the B.E., M.E., and Ph.D. degrees in applied physics from Waseda University, Japan, in 1990, 1992, and 1996, respectively. He is currently a Deputy Director and a Team Leader at the Sensing System Research Center (SSRC), National Institute of Advanced Industrial Science and Technology (AIST), Tsukuba, Japan. His research interests include solid-state material physics and its applications, particularly smart materials, including the preparation of ferroelectric and piezoelectric materials and their application in the field of the IoT sensing. He is now engaged in research projects to develop a useful sensor fusion systems, including smart materials, for applications in a smart society.